

Ulrich Sauter
17-935-966

Gain characterization of pump DBR VECSEL in the 2- μm range

Semester project

Ultrafast Laser Physics, Prof. Ursula Keller
Department of Physics, Institute for Quantum Electronics
Swiss Federal Institute of Technology Zürich

Supervision

Marco Gaulke

June, 2023

Abstract

A novel optically-pumped vertical external cavity surface emitting laser (VECSEL) operating in the 2 μm spectral range

In order to gain deeper insights into the impact of VECSEL design (?MENTION WHAT CHANGES IN DESIGN?), it is necessary to measure the characteristic parameters of the VECSEL under various conditions. This involved utilizing an existing setup and control software to measure these parameters at various temperatures and pump powers. To enhance efficiency and save valuable measurement time, the setup was further improved by adding the possibility to control and automate the pump diode power, as well as further improvement to the stability and detection algorithm of the software.

Contents

Abstract	I
1 Introduction	1
1.1 Gain saturation	2
2 Methods	4
2.1 VECSEL Chips	4
2.2 Experimental setup	6
2.2.1 Automation of the pump power	8
2.3 Signal processing algorithm	9
3 Results & Discussion	11
3.1 Saturation fluence F_{sat}	12
3.2 Small signal reflectivity R_{ss}	13
3.3 Rollover parameter F_2	14
3.4 Comparision to previous work	15
4 Conclusion	16
A Appendices	19
A.1 Measurement and fitting data	19
A.1.1 No pump DBR VECSEL	19
A.1.2 Copper, pump DBR VECSEL	21
A.1.3 Diamond, pump DBR VECSEL	23
A.1.4 Hybrid VECSEL	25

Chapter 1

Introduction

Semiconductor lasers present a very compact compact, efficient and mass producible solid state laser. They have many applications in everyday life and science, such as optical communication, data storage, printing, sensing, medical treatment, and pumping solid-state lasers.

A special type of semiconductor laser is a VECSEL (Vertical External Cavity Surface Emitting Laser). It is based on a VCSEL (Vertical Cavity Surface Emitting Laser) and emits light perpendicular to the surface of a semiconductor wafer but unlike a VCSEL, a VECSEL has an external cavity that is formed by one or more optical elements outside the wafer. This allows for more flexibility in designing the laser parameters, such as wavelength, output power, beam quality and pulse duration. VECSEL are also typically optical pumped whereas VCSEL are electrically pumped.

The basic structure of the VECSEL itself consists of an active region and a distributed Bragg reflector (DBR). Inside the active region, multiple quantum wells are located which are engineered to provide the necessary energy levels for the desired wavelength of laser emission, in this case the 2- μm range. This wavelength range is of strong interest for many application, particularly for medical purposes and atmospheric spectroscopy. The DBR is made of alternating layers of semiconductor material with different refractive indices. By choosing the optical layer thicknesses to be one quarter of the laser wavelength, the DBR achieves high reflectivity at the desired wavelength range of the laser.

A novel design approach incorporates a DBR for the pump wavelength as well. This new structure shows remarkable improvements in terms of efficiency and power scaling in continuous wave (CW) operation, as seen in Fig. 1.1. The performance improvements in a modelocked configuration were not as significant. To get a better understanding of this, additional investigation were conducted and for this work we focused on the gain saturation characteristics.

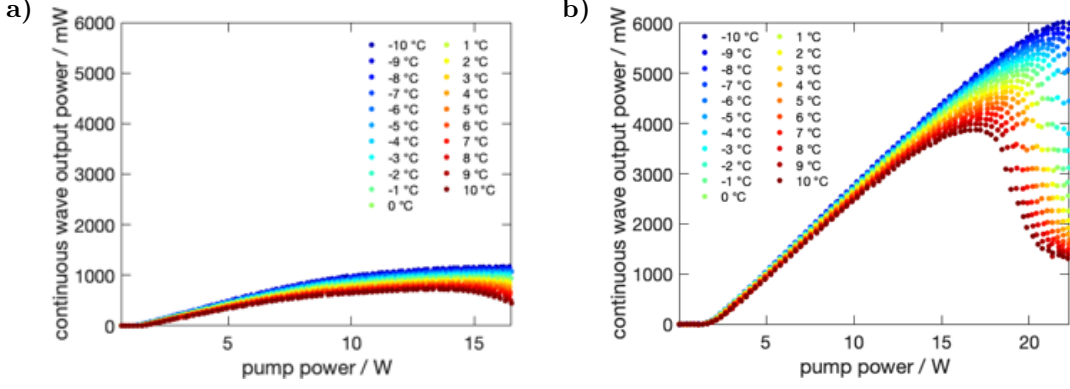


Figure 1.1: Continuous wave (CW) output power of a VECSEL without pump DBR a) and with pump DBR b) versus pump power under different heat sink temperature ranging from -10°C to 10°C . The data demonstrates the effect of the pump DBR on the power scaling performance in CW operation. The VECSEL with pump DBR shows an increase of 18 % in efficiency and a sixfold increase in output power.

1.1 Gain saturation

Gain saturation describes a phenomenon that occurs when the active region of a laser is unable to maintain its gain as the pump power increases for high values.

To study this behaviour, one measures the nonlinear behaviour of the reflectivity for an increasing amount of probe fluence, as can be seen in Fig. 1.2. To quantify this behaviour and gain some macroscopic parameters, a model based on the saturation of the absorber in a SESAM can be fitted to the data.

$$R(F) = R_{ns} \frac{F_{sat}}{F} \ln \left\{ 1 + \frac{R_{ss}}{R_{ns}} \left[\exp \left(\frac{F}{F_{sat}} \right) - 1 \right] \right\} \exp \left(-\frac{F}{F_2} \right) \quad (1.1)$$

The parameters from Eq. (1.1) are the saturation fluence F_{sat} , the small signal reflectivity R_{ss} , the nonsaturable reflectivity R_{ns} and the rollover parameter F_2 .

The saturation fluence F_{sat} is the fluence at which the reflectivity reduces to $1/e$ of its maximum. It also represents the point at which the population inversion inside the active region becomes saturated, therefore it is closely tied to the material properties of the active region.

The small signal reflectivity R_{ss} refers to the reflectivity at low probe fluence, where the gain is not significantly saturated. In this regime nonlinear effects are minimal and the reflectivity can be considered to be in the linear regime and the small signal approximation can be applied and the small signal gain can be calculated as $g_{ss} = R_{ss} - 100\%$.

The nonsaturable reflectivity R_{ns} arises from absorption and scattering at im-

purities and interfaces inside the VECSEL structure. This limits the maximum performance of the VECSEL, thus reducing defect density during the growing process is important. Since this effect is associated with imperfection and reflection inside the structure it remains relatively constant for different probe fluences.

The rollover parameter F_2 describes further absorption from two photon absorption or higher order effects resulting in a strong decrease in the reflectivity at high fluences.

Figure 1.2 shows the key parameters and the fitted model with and without accounting for the rollover for a measurement of a VECSEL with an integrated pump DBR.

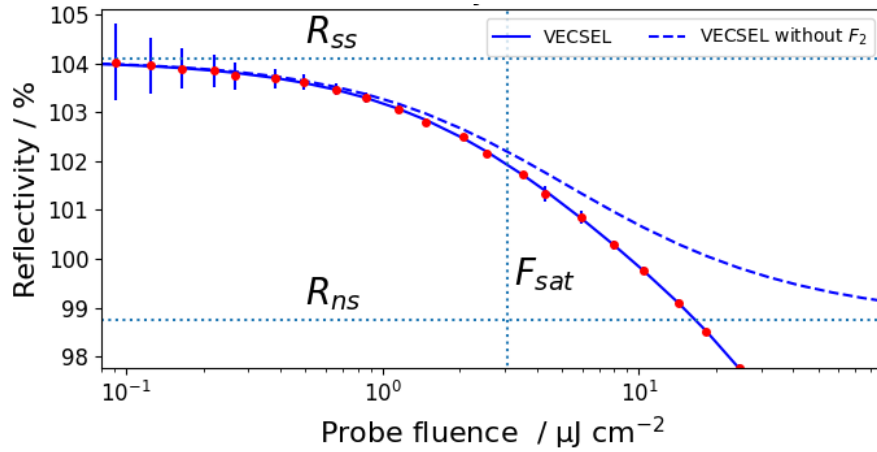


Figure 1.2: Nonlinear reflectivity measurement for a VECSEL with integrated pump DBR and diamond heat spreader versus probe fluence. The data is shown with the fitted model utilizing Eq. (1.1) and the same model without the rollover parameter F_2 . Additionally the different parameters R_{ss} , R_{ns} and F_{sat} are visualized.

Chapter 2

Methods

In order to accurately determine the characteristic parameters of a VECSEL chip, it is necessary to have an experimental setup that can measure a small change, in the order of 0.1 % in the reflectivity over a dynamic range of about 4 order of magnitude in pulse fluence. A dedicated setup fulfilling these criteria has been constructed and utilized by (INSERT HERE REFERENCES).

For the measurements, a total of 4 different VECSEL chip were used, with three of them having a different structure (further discussed in Section 2.1). We were interested on the impact of different pump powers and the temperatures on the characteristic parameters of the VECSEL across the three different structures. For this we measured the nonlinear reflectivity for each chip for 9 different pump powers in the range from 0 W to 16 W and for three temperatures -10°C , 0°C and 10°C .

The subsequent section provide an overview of the different VECSEL structures, the measurement setup and the data processing method.

2.1 VECSEL Chips

The basic structure of a VECSEL gain chip is shown in Fig. 2.1. The main feature of the structure are as follows:

- Heat spreader: The heat spreader role is in dissipating the heat generated during the operation of the VECSEL chip to a Peltier-controlled copper heat-sink.
- Pump & laser DBR: The purpose of the two bottom mirrors is to reflect the laser light and the pump light. There are two main advantages to this approach: firstly, because of higher absorption, there is a higher optical-to-optical efficiency due to the two passes through the active region, and

secondly, there is less absorption in the mirror and in the heat sink, which results also in a higher efficiency and a higher maximum output power. The high reflectivity for two wavelengths is realized by using a distributed Bragg reflector (DBR)

- Active region: The purpose of the active region is the conversion of the pump light into the laser light. The gain medium in the active region is often composed of quantum wells or quantum dots.
- Anti-reflection coating: The anti-reflection section is optimized to reduce the otherwise large reflection from the air/GaAs interface

The three VECSEL chip structures used for this work are described below.

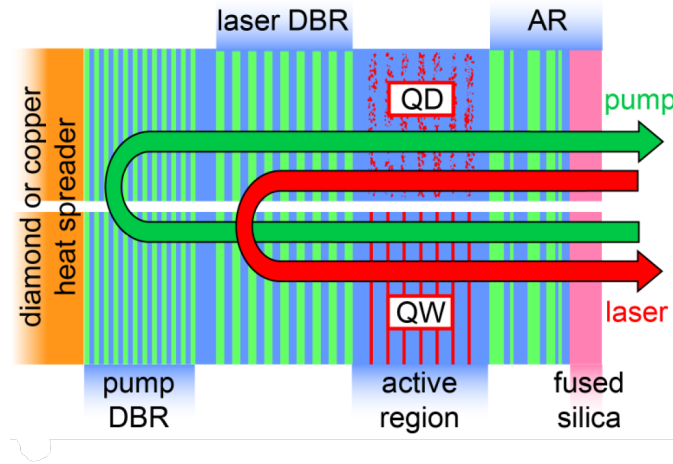


Figure 2.1: TODO: caption

No pump DBR chip, SV166

This structure has an antiresonant design and cooled from the backside by a copper heat spreader. The DBR consists of 19-pairs of GaSb/AlAs_{0.08}Sb_{0.92} layers design around a wavelength of 2080 nm. The active region has 5×3 In_{0.27}Ga_{0.73}Sb quantum wells (QW) placed at the maximum of the standing-wave cavity. Additional barriers layer made of AlAs_{0.08}Sb_{0.92} are placed around the gain QW to increase the photoluminescence. The last layer is a PECVD coating made of Si₃N₄, which serves as an anti-reflection coating.

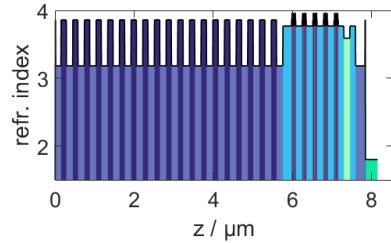


Figure 2.2: Design of the no pump DBR chip.

Pump DBR chip, SV167

This is a similar structure as above but this time including an extra DBR for the pump wavelength of 1470 nm. The pump DBR is made of 10 layers of $\text{Al}_{0.2}\text{As}_{0.8}\text{Sb}/\text{Al}_{0.15}\text{Ga}_{0.85}\text{AsSb}$. For the thickness of the layers the 45° incident of the pump beam had to be accounted for. This structure was measured twice but for different heat spreaders, one made of copper and the other of diamond, to observe and compare the influence of better thermal conductivity of the heat spreader.

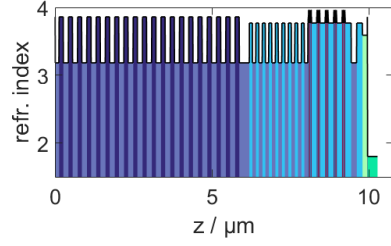


Figure 2.3: Design of the pump DBR chip.

Hybrid chip, SV165

This structure incorporated a hybrid metal-semiconductor Bragg reflector. It consisted of a 100 nm copper layer with 10.5 $\text{AlAs}_{0.08}\text{Sb}_{0.92}/\text{GaSb}$ layers. This allows for a thinner gain chip design of just under $5\text{ }\mu\text{m}$ compared to the other structures $7.5\text{ }\mu\text{m}$ resp. $10\text{ }\mu\text{m}$ for the pump DBR design. This lowered the thermal resistance of the device by 24 %. This structure also has a different design for the active region. The cladding layer between the pump absorbing layers is made of GaSb to allow for barrier pumping.

2.2 Experimental setup

The experimental setup is depicted in Fig. 2.5. The setup is driven by a modelocked Ti:sapphire laser. The laser emits femtosecond pulses at a wavelength of 810 nm, with a repetition rate of 80 MHz and an average output power of 4 W. The laser beam then passes through an optical parametric oscillator (OPO), where the beam undergoes nonlinear frequency conversion resulting in two outputs: an idler wave and a signal wave. The OPO idler wave can be tuned from $1.7\text{ }\mu\text{m}$ to $4\text{ }\mu\text{m}$ and has a maximum output power of 650 mW. The idler has been tuned to a specific wavelength of 2071.7 nm and was stabilized using an integrated automated feedback loop.

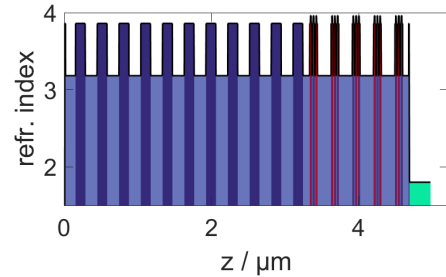


Figure 2.4: Design of the hybrid chip

To further achieve a wide range of pulse fluences, the laser beam is directed through two wire-grid polarizers. One of the polarizers is placed on a controllable rotation stage to adjust the beam attenuation. The wire-grid polarizers have a

broad range of attenuation across different wavelengths and do not alter the beam path during rotation. After the attenuation stage, the beam passes through a beamsplitter, which separates it into two arms: the reference arm and the sample arm.

The reference arm contains a high-reflection mirror of known reflectivity from which the leaking signal is collected in a photodiode to monitor the fluence during a measurement. The VECSEL chip is placed at the end of the sample arm. Before the beam is incident on the VECSEL, a focusing lens is used to achieve higher fluences on the VECSEL. The VECSEL is probed under normal incidence angle, and its reflection is collected using the same lens. Both beams are recombined at the beamsplitter and directed to an integrating sphere photodiode to measure the total reflected power. The pump beam enters and shines on the VECSEL at a 30° angle and is shown in green.

To measure the different signals from the two different arms and also measure the photoluminescence (PL) signal of the pumped VECSEL chips, two choppers are used. The two choppers separate the signals in time allowing to measure the signals with the same detector. The choppers are phase locked and chopper 2 is run at half of the frequency of chopper 1, specifically at 55 Hz. Chopper 2 is placed in the beam path before the attenuator to block the beam during every second cycle of chopper 1. This allows to isolate the PL signal. Chopper 1 is placed such that both arms can be intercepted by the blades, enabling the passage of light from both or either of the arms. During one cycle of chopper 2, five distinct states can occur, each allowing for a different measurement configuration:

1. Only the sample signal, composed of the photoluminescence and the sample signal (S+PL)
2. Both arms are open, allowing the combined signal from the sample and reference arm (S+PL+M)
3. Only the reference signal (M)
4. Both arms are blocked and only the background signal from the detector is measured (Z)
5. The probe beam gets blocked and only the (PL) signal is measured

To obtain the reflectivity from the VECSEL, the (PL) and the background signal (Z) are subtracted from the sample signal (S+PL). The resulting value is then compared to the reference measurement (M). This yields a scaling factor R , which then can be used to calculate the reflectivity based on the known reflectivity of the reference mirror. To obtain accurate measurement points, 200 such signal iterations are averaged together for the final measurement point.

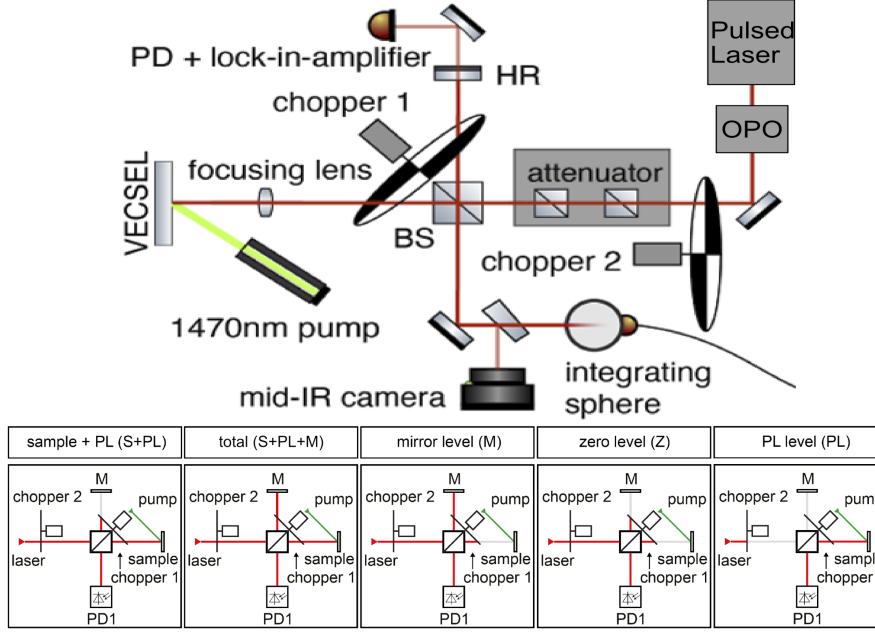


Figure 2.5: On top: Experimental Setup for gain characterization of VECSEL chips. The laser source is a tunable optical parametric oscillator pumped by a modelocked Ti:sapphire laser. An attenuation stage controls the incident probe fluence on the VECSEL. The pump beam enters the setup at a 30° angle. Two choppers, phase-locked and operating at different frequencies, are positioned to differentiate signals and measure photoluminescence (PL) emitted by the pumped VECSEL chip. The figure showcases the key components and their relative positions within the experimental setup. On bottom: Visualization of the five different configurations of the two choppers and the measured signal, adjusted from REFERENCE.

2.2.1 Automation of the pump power

To improve the time efficiency and increase the unattended measuring time of the experimental setup, the control of the pump power has been automated. In the original setup, the pump power of the laser diode was controlled over a Delta Elektronik SM 18-50 DC power supply, which can deliver up to 50 A at up to 18 V. The power supply was connected over a serial interface controller to a computer and integrated into the already existing user interface of the measurement setup. To implement the control of the pump, a new text field has been added to the user interface where a list of current values for the power supply can be added. Instead of specifying power values directly, the decisions made to enter current values instead due to the potential for exchanging the pump laser diode in the future, which would necessitate to adjust the controller in the software. The software then iterates over this list and makes a complete measurement for each current value in the list. However, the full automation also required to adjust the signal processing algorithm of the software, which will be discussed in the next section.

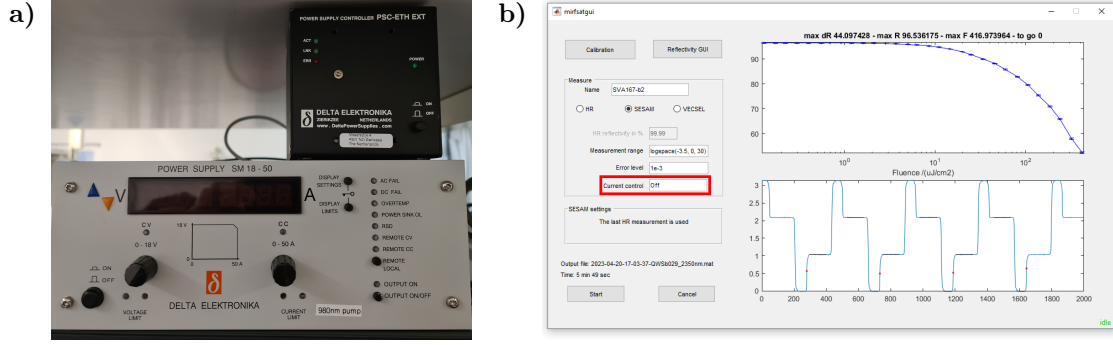


Figure 2.6: TODO: ADJUST SOFTWARE PICTURE AND WRITE CAPTION

2.3 Signal processing algorithm

In Fig. 2.7 the signal of the photodiode is shown for one cycle of chopper 2, as described in Section 2.2. The five signal levels resulting from the different chopper configuration are clearly distinguishable. To process the signal, the following algorithm had been used. Initially, for example at 97%, the software identifies trigger points when the signal falls below this level. Ideally, the triggering occurs at the falling edge of the total signal peak. The software utilizes these trigger points to determine the locations of the other signal levels and calculates the mean values of the flat levels. From these the software computes the sample reflectivity using the method outlined at the end of Section 2.2.

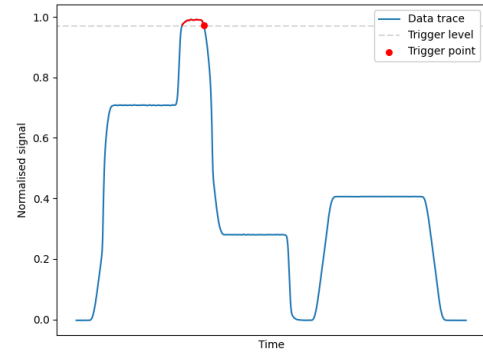


Figure 2.7: Illustration of original algorithm

However, this method exhibits some limitations when used for the automation for the setup. These limitations arise from the possibility to have multiple triggers in a single cycle, resulting in unusable measurement data and necessitating to manually adjusting the trigger and redoing the measurement. Such a manual process is counter productive to the aim of automation. To address this issue, it is essential to investigate the underlying causes.

For one, there is the nature of the measured signal. Since all levels are measured simultaneously and with the same detector, their signal strength are in relation to each

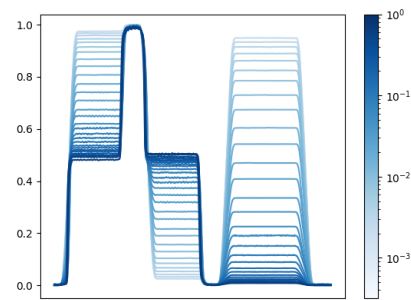


Figure 2.8: Signal for a fixed pump power and increasing amount of fluence. (NEED TO ADD AXIS LABEL TO IMAGE)

other. As a result, high variations in signal levels occur during a measurement, as illustrated in Fig. 2.8. Since measurements are conducted for different pump powers, the influence of the PL has to be taken into account. Initially, at low probe fluences, the PL signal dominates, requiring to set a trigger level to ensure triggering on the total level rather than the PL level.

To address these mistriggering cases, the following method has been implemented which has also been illustrated in Fig. 2.9. By utilizing the approach described above but with a lower triggering value of 80 %, avoids triggering on a noisy total level but allows for triggering on both the total peak and the PL peak. Additionally, this introduces the risk of triggering on a noisy signal level that may lay close to the trigger level during a measurement. To address this, neighbouring points (small red dots in Fig. 2.9) of the triggers are examined and ensuring that the signal level is descending. Finally, we verify that we are on the total peak by requiring that a maximum value of the signal is in close proximity (orange shaded area in Fig. 2.9) to the trigger point.

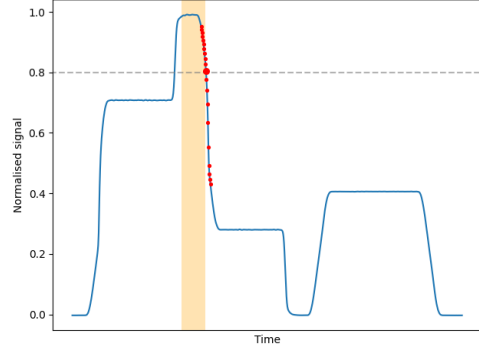


Figure 2.9: Illustration of improved algorithm

Using this method allowed for the automated measurement process to successfully be finished. Resulting in a decrease of 5% in measurement time and the fully autonomous measuring of data over arbitrary number of pump powers.

Chapter 3

Results & Discussion

To asses and compare the different structures, we use the fitting parameters obtain from the model in Eq. (1.1). To account for parameter correlations, we first determined the non-saturable reflectivity by fitting the measurement with no pump power and then fixed the parameter for subsequent fits. This approach ensured that the fitting process accurately captures that the nonsaturable reflectivity stems from impurities of the structure, which don't change during a measurement. Additionally, we restriced the fitting range for high pulse fluences. This was motivated by the nonlinear behaviour of the reflectivity observed at high fluence levels, where the behavior of the system becomes more complex and less understood.

In the subsequent sections, we go over of each of the three remaining fitting parameters. We explain the general trends and features of the measurements on the basis of the results for the copper heat spreader with pump DBR (cDBR) VECSEL design and then discuss these feature for the other structures. All the fitting parameters can be found in Appendix A.

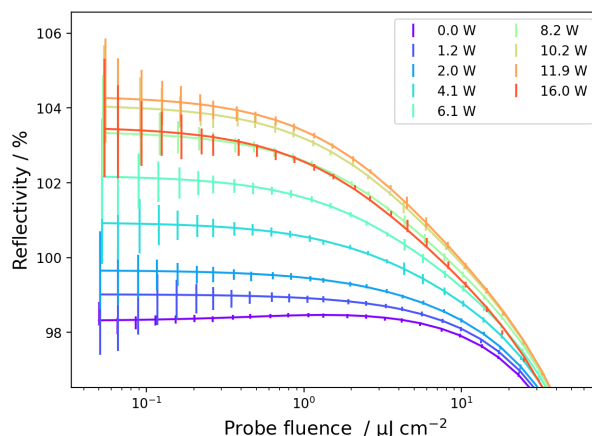


Figure 3.1: Nonlinear reflectivity measurement for nine different pump powers of the pump DBR VECSEL with the copper heat spreader at 0°C. The data has been fitted with the model from Eq. (1.1).

3.1 Saturation fluence F_{sat}

Results

In Fig. 3.2, the saturation fluence of the cDBR VECSEL for three different heatsink temperatures. Initially, at zero pump power, the saturation fluences are relatively low. But as soon as population inversion is reached within the gain region, the saturation fluence stays at a constant value. Before reaching the constant plateau, there is often a jump in the observed saturation fluence. This jump can be attributed to an artifact from the fitting process. The flat reflectivity curve at low pump powers (see Fig. 3.1 for 1.2 W), makes it challenging for the fitting method to accurately determine the saturation fluence.

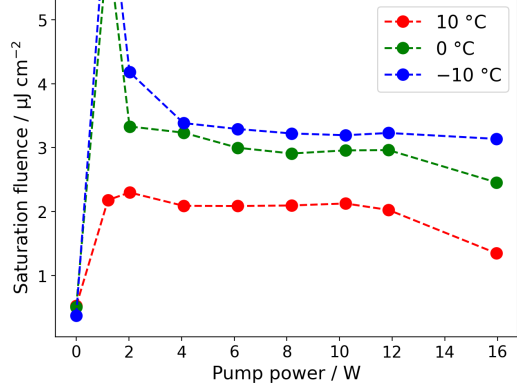


Figure 3.2: Saturation fluences for the pump DBR VECSEL with a copper heat spreader.

Regarding the temperature dependence we see that we get a higher saturation fluence for colder temperatures, which may appear counterintuitive considering that the carrier density decreases for lower temperatures. The explanation for this can be found in the design of the VECSEL. The optical thicknesses in the structure are design for a specific wavelength, but thermal expansion can alter the thicknesses and therefore the specific wavelength of the design. As the measurements are performed for a fixed wavelength, the temperature can affect how much we are on resonance, hence modifying how efficient carriers can be promoted and therefore the observed saturation fluence. This nonlinear behaviour is also reflected in the data.

Discussion

In Table 3.1 the mean values of the saturation fluences of the different structures and temperatures can be seen. The mean values were evaluated for data points with pump powers exceeding 4 W to minimize the influence of the fitting artifact.

Comparing the no pump DBR VECSEL to the cDBR VECSEL, no significant difference in the saturation fluence of the two structures is observed. This is reasonable considering that both chips have the same active region.

If we compare the two VECSEL with pump DBRS we see that for 10 °C they have the same saturation fluence. But for colder heat sink temperatures the VECSEL with the diamond heat spreader (dDBR) has a higher saturation fluence.

3.2. SMALL SIGNAL REFLECTIVITY R_{ss}

This can be attributed to the improved thermal conductivity of the diamond heat spreader, resulting in a more efficient cooling of the structure. Consequently, the thermal expansion is also more significant and shifting the resonance of the structure enough to be more inline with the probing wavelength, therefore reaching a higher saturation fluence.

The hybrid VECSEL shows a different result compared to the others. In this case, cooling the structure moves the resonance of the design farther away from the probing wavelength, decreasing the saturation fluence.

Heat sink temperature	Saturation fluence $F_{sat} / \mu\text{J cm}^{-2}$		
	10 °C	0 °C	−10 °C
No pump DBR	1.9 ± 0.2	3.5 ± 0.2	3.7 ± 0.1
Copper, pump DBR	2.08 ± 0.04	2.96 ± 0.03	3.23 ± 0.04
Diamond, pump DBR	1.93 ± 0.04	4.0 ± 0.3	4.3 ± 0.3
Hybrid	4.5 ± 0.2	1.83 ± 0.02	1.60 ± 0.03

Table 3.1: This table displays the mean saturation fluence values for the four VECSEL chips for the three heat sink temperatures. For the mean, only the values after the VECSEL achieved population inversion were used.

3.2 Small signal reflectivity R_{ss}

Results

Fig. 3.3 shows the small signal reflectivity for the cDBR VECSEL for the three different heatsink temperatures. We see that the small signal reflectivity initially exhibits a linear growth but then drops off for higher pulse fluences. This break off tends to happen for higher fluence values for colder temperatures.

Notably for this measurement of the cDBR VECSEL, we see that the chips performance in terms of maximum reflectivity is higher compared to the colder temperatures. This can be most likely attributed to spatial variation in the measurement spot on the chip. Consequently, comparing maximum reflectivity values across different VECSEL lacks significance. Instead, we adopted a different approach to compare the chips by characterizing the break-off behaviour.

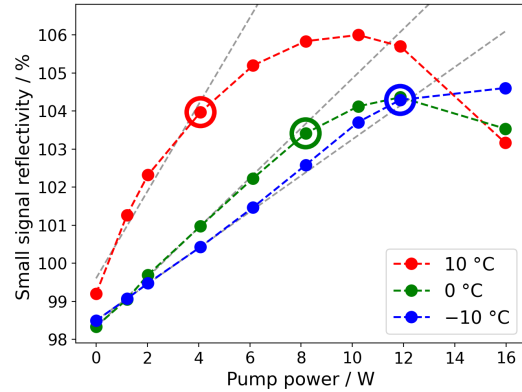


Figure 3.3: Small signal reflectivity for the copper heat spreader pump DBR VECSEL. The break-off points are marked by circle around the data point.

3.3. ROLLOVER PARAMETER F_2

For this, a linear regression for the first four data points was applied. The break-off point was determined as the power of the data point before deviating from the linear regression, referred to as the break-off power P_{off} .

Discussion

In Table 3.2 the break-off power P_{off} and the maximum reflectivity R_{max} are listed for the different VECSEL and heat sink temperatures. Comparing the different break-off powers to each other There is no significant difference between the no pump DBR chip and the pump DBR chip. However, it shows that the break-off happens sooner for the diamond heat spreader than the copper, contrary to our expectation. This could be explained if we are limited with our gain by the material properties of the gain region and not some thermal effects, which could be investigated in the future. As for the maximum reflectivity, we observe that the dDDR chip shows overall higher performance compared to the with a maximum small signal reflectivity of 106.5 %.

Heat sink temperature	10 °C		0 °C		−10 °C	
	P_{off}	R_{max}	P_{off}	R_{max}	P_{off}	R_{max}
No pump DBR	4	102.5	8	103.4	12	103.4
Copper, pump DBR	4	106.0	8	104.4	12	104.6
Diamond, pump DBR	4	105.3	6	106.2	10	106.5
Hybrid	6	103.5	10	103.6	12	103.7

Table 3.2: Break off power and maximum reflectivity values for the different measurement configurations.

3.3 Rollover parameter F_2

Results

In Fig. 3.4 one can see the rollover parameter for the cDBR VECSEL. After reaching population inversion, we see a linear decrease of the rollover parameter for higher pump powers. This decrease in the rollover means, that for higher pump powers, we get a higher likelihood of two photon absorption in the active region. This could be explained by the heating of the active region from the pump and the increase of the two-photon absorption rate with temperature.

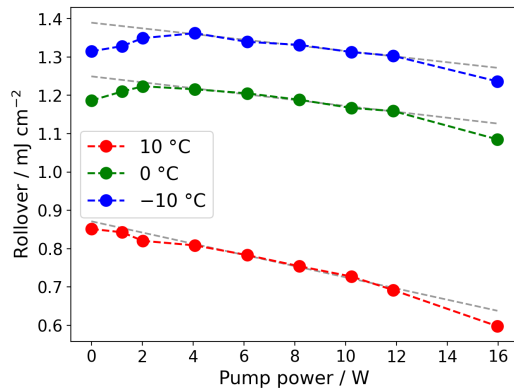


Figure 3.4: Rollover parameter for the copper heat spreader pump DBR VECSEL with linear fits.

3.4. COMPARISON TO PREVIOUS WORK

As for the temperature dependence we see that we have a higher value for colder temperatures, which also aligns with the temperature dependence of the two photon absorption.

Discussion

In Table 3.3 the fit parameters of a linear fit ($mx + b$) are listed for the different VECSEL chips and heat sink temperature. For the fit, we excluded the first three points, as we did for the saturation. If we compare the slopes of the different fits, no clear trend is observable, except that the slope has a negative sign.

Comparing the no pump DBR VECSEL with the pump DBR VECSEL we see that the no pump DBR VECSEL has almost double the rollover value.

Heat sink temperature linear fit parameters	10 °C		0 °C		−10 °C	
	$m \cdot 10^3$	b	$m \cdot 10^3$	b	$m \cdot 10^3$	b
No pump DBR	-15.16	1.83	-18.47	2.68	-19.50	2.96
Copper, pump DBR	-14.62	0.87	-7.71	1.25	-7.38	1.39
Diamond, pump DBR	-9.21	0.93	-5.19	1.54	+5.62	1.55
Hybrid	-0.35	5.33	-21.1	2.72	-7.98	2.23

Table 3.3: Linear fit parameters of the saturation fluence.

3.4 Comparison to previous work

If we want to compare our results to previous work. We can only do that for the no pump DBR VECSEL, since for the other structures no gain saturation measurements were done before. We can look at the work of Marco Gaulke et al. Their results and ours can be seen in Table 3.4. The fit parameters indicating consistency between the two studies. We also observe the same constant behavior between saturation fluence and pump power as reported in the paper.

Moreover, our investigation highlights a notable advancement in small signal gain for the new structure incorporating a pump DBR and diamond heat spreader. We achieve a record small signal gain of 6.5 %, surpassing the previously reported value of 6.5 %. This improvement signifies the enhanced performance and potential of the new structure in achieving higher gain.

	previous work at 5 °C	this work at 10 °C
Saturation fluence $F_{sat} / \mu\text{J cm}^{-2}$	2.06 ± 0.11	1.9 ± 0.2
Small signal Reflectivity $R_{ss} / \%$	103.5	102.5
Nonsaturable reflectivity $R_{ns} / \%$	0.98 ± 0.12	0.99
Rollover parameter $F_2 / \mu\text{J cm}^{-2}$	2.01 ± 0.065	1.83

Table 3.4: Comparison of the no pump DBR VECSEL parameters to the previous work of Marco Gaulke et al.

Chapter 4

Conclusion

In conclusion, we assessed and compared different VECSEL chips based on their gain saturation at different temperatures.

Structures involved using fitting parameters obtained from the model described in Equation (eq:model). To account for parameter correlations, we initially determined the non-saturable reflectivity by fitting the measurement with no pump power and then fixed the parameter for subsequent fits. This approach ensured that the fitting process accurately captured the non-saturable reflectivity originating from impurities in the structure, which remain unchanged during measurements. Additionally, we restricted the fitting range for high pulse fluences due to the complex and less understood nonlinear behavior observed in the reflectivity at high fluence levels.

In the subsequent sections, we examined each of the three remaining fitting parameters. We discussed the general trends and features of the measurements based on the results for the copper heat spreader with pump DBR (cDBR) VECSEL design and subsequently explored these features for the other structures.

Regarding the saturation fluence (F_{sat}), we analyzed its behavior for the cDBR VECSEL at different heatsink temperatures. We observed that the saturation fluence remained relatively low initially at zero pump power and then reached a constant value once population inversion was achieved within the gain region. However, before reaching the constant plateau, there was often a jump in the observed saturation fluence, which could be attributed to an artifact from the fitting process. The flat reflectivity curve at low pump powers made it challenging for the fitting method to accurately determine the saturation fluence.

Regarding temperature dependence, we found that colder temperatures resulted in higher saturation fluence, which might appear counterintuitive considering the decrease in carrier density at lower temperatures. However, the explanation lies in the design of the VECSEL. The optical thicknesses in the structure are designed for a specific wavelength, but thermal expansion can alter these thicknesses, consequently affecting the specific wavelength of the design. As the measurements

were performed for a fixed wavelength, temperature variations influenced the resonance condition and, thus, the efficiency of carrier promotion, leading to observed changes in saturation fluence. This nonlinear behavior was also evident in the data.

Comparing the mean values of saturation fluence for the different structures and temperatures (see Table tab:fsat), we found no significant difference between the no pump DBR VECSEL and the cDBR VECSEL, which is reasonable considering that both chips have the same active region.

In the case of VECSELs with pump DBRs, comparing the cDBR VECSEL to the diamond heat spreader (dDBR) VECSEL, we observed that at 10°C, they exhibited similar saturation fluence. However, at colder heatsink temperatures, the dDBR VECSEL showed a higher saturation fluence. This can be attributed to the improved thermal conductivity of the diamond heat spreader, leading to more efficient cooling of the structure. As a result, thermal expansion becomes more significant, shifting the resonance of the structure closer to the probing wavelength and thereby increasing the saturation fluence.

The hybrid VECSEL yielded different results compared to the other structures. Cooling the structure in this case moved the resonance of the design further away from the probing wavelength, resulting in a decrease in saturation fluence.

In summary, our analysis of saturation fluence revealed temperature-dependent behavior and highlighted the influence of different heat spreader materials on the saturation fluence of the VECSEL structures. The results underscored the importance of considering thermal effects and their impact on resonance conditions and overall device performance.

Conclusion:

In this chapter, we assessed and compared different VECSEL structures using fitting parameters obtained from our model. We adopted an approach that accounted for parameter correlations and considered the non-saturable reflectivity by fixing the parameter obtained from fitting the measurement with no pump power. We also restricted the fitting range for high pulse fluences due to the complex and less understood behavior of the system at high fluence levels.

Firstly, we discussed the saturation fluence (F_{sat}) parameter. We observed that the saturation fluence remained constant once population inversion was reached, but there was often a jump in the observed saturation fluence before reaching the constant plateau. We attributed this jump to an artifact from the fitting process. Additionally, we found that the saturation fluence increased with colder temperatures, which may seem counterintuitive considering the decrease in carrier density. However, this behavior can be explained by the thermal expansion-induced shift in resonance, affecting the efficiency of carrier promotion.

Next, we analyzed the small signal reflectivity (R_{ss}) parameter. We observed a linear growth in the small signal reflectivity initially, followed by a drop-off at

higher pulse fluences. This break-off point occurred at higher fluence values for colder temperatures. We noted that comparing the maximum reflectivity values across different VECSEL chips lacked significance due to spatial variation in the measurement spot. Instead, we focused on characterizing the break-off behavior and found no significant difference between the no pump DBR and pump DBR chips. Surprisingly, the break-off happened sooner for the diamond heat spreader compared to the copper heat spreader.

Finally, we examined the rollover parameter (F_2) and observed a linear decrease in its value for higher pump powers. This decrease indicated a higher likelihood of two-photon absorption in the active region. We also found that the rollover parameter had a higher value for colder temperatures, consistent with the temperature dependence of two-photon absorption.

Comparing our results with previous work, we could only make comparisons for the no pump DBR VECSEL. The fit parameters indicated consistency between our study and the previous work, and we observed the same constant behavior between saturation fluence and pump power as reported in the paper.

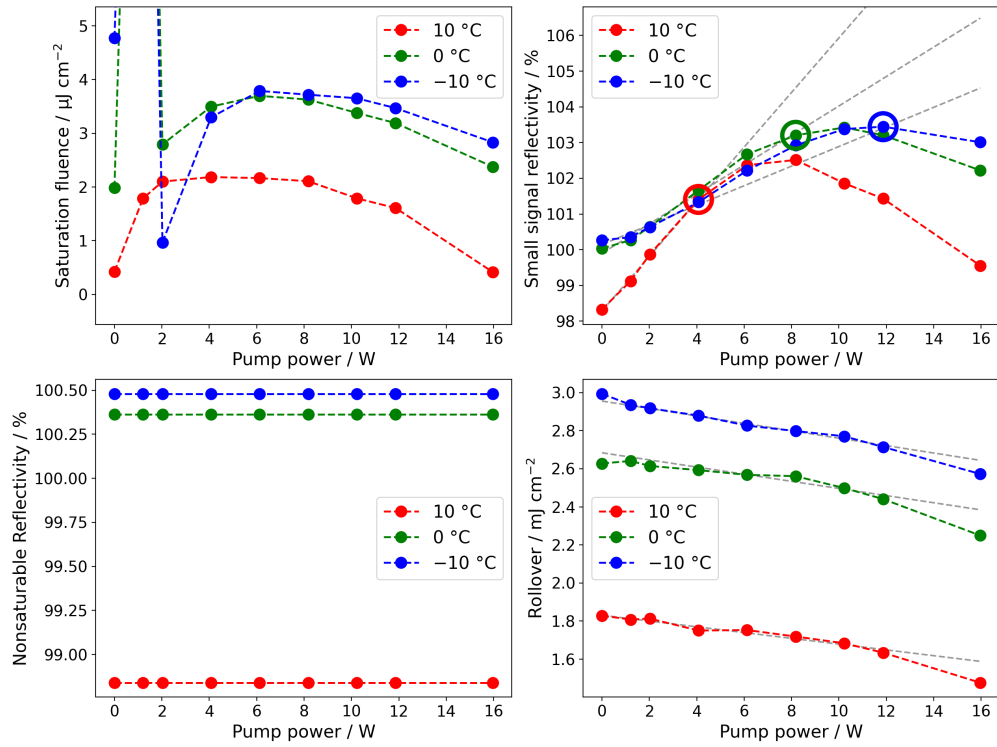
Overall, our investigation provided insights into the performance and characteristics of different VECSEL structures. We observed the influence of temperature, thermal effects, and material properties on the fitting parameters. Furthermore, our results highlighted the improved performance of the new structure incorporating a pump DBR and diamond heat spreader, achieving a record small signal gain. These findings contribute to the understanding and potential advancement of VECSEL technology.

Appendix A

Appendices

A.1 Measurement and fitting data

A.1.1 No pump DBR VECSEL



Power / W	$F_{sat} / \mu Jcm^{-2}$	$R_{ss} / \%$	$R_{ns} / \%$	$F_2 / \mu Jcm^{-2}$
0.0	0.4242817	98.32646	98.83956	1828.769
1.2	1.788391	99.12145	98.83956	1808.165
2.0	2.101345	99.87338	98.83956	1812.988
4.1	2.184542	101.408	98.83956	1750.382
6.1	2.165731	102.3672	98.83956	1752.908
8.2	2.107595	102.5144	98.83956	1718.818
10.2	1.789862	101.8599	98.83956	1683.561
11.9	1.608349	101.4312	98.83956	1634.176
16.0	0.4177362	99.55455	98.83956	1476.493

Table A.1: Fitting parameters for no pump DBR at 10 °C

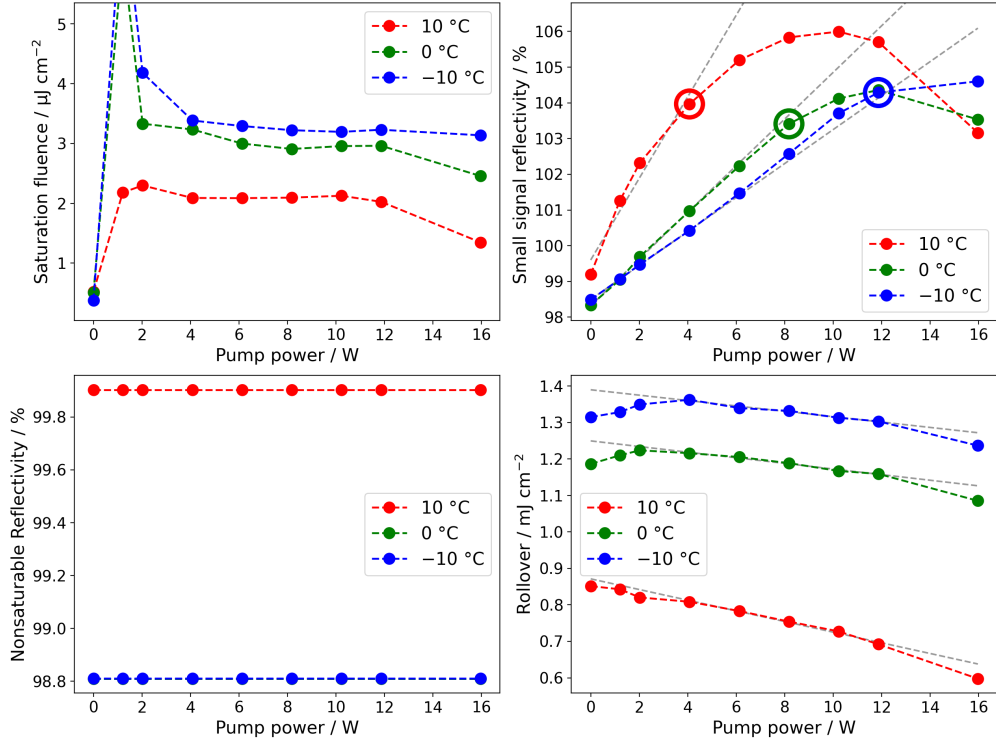
Power / W	$F_{sat} / \mu Jcm^{-2}$	$R_{ss} / \%$	$R_{ns} / \%$	$F_2 / \mu Jcm^{-2}$
0.0	1.98311	100.0328	100.3635	2627.521
1.2	20.0	100.2707	100.3635	2640.861
2.0	2.792377	100.6464	100.3635	2614.563
4.1	3.495024	101.6619	100.3635	2592.491
6.1	3.6954	102.6746	100.3635	2567.857
8.2	3.625693	103.2034	100.3635	2560.939
10.2	3.378039	103.4231	100.3635	2498.461
11.9	3.188481	103.2076	100.3635	2440.667
16.0	2.374694	102.2209	100.3635	2249.402

Table A.2: Fitting parameters for no pump DBR at 0 °C

Power / W	$F_{sat} / \mu Jcm^{-2}$	$R_{ss} / \%$	$R_{ns} / \%$	$F_2 / \mu Jcm^{-2}$
0.0	4.771398	100.2647	100.4798	2993.587
1.2	20.0	100.3514	100.4798	2935.761
2.0	0.969857	100.636	100.4798	2917.388
4.1	3.295232	101.3324	100.4798	2879.026
6.1	3.786001	102.2179	100.4798	2826.371
8.2	3.716613	102.9223	100.4798	2797.888
10.2	3.650727	103.3792	100.4798	2770.251
11.9	3.467088	103.4452	100.4798	2714.26
16.0	2.83112	103.0094	100.4798	2572.357

Table A.3: Fitting parameters for no pump DBR at −10 °C

A.1.2 Copper, pump DBR VECSEL



Power / W	$F_{sat} / \mu\text{Jcm}^{-2}$	$R_{ss} / \%$	$R_{ns} / \%$	$F_2 / \mu\text{Jcm}^{-2}$
0.0	0.5243558	99.19443	99.90335	851.3778
1.2	2.180054	101.2653	99.90335	842.6771
2.0	2.299238	102.3185	99.90335	820.2702
4.1	2.090052	103.9689	99.90335	808.4475
6.1	2.086848	105.196	99.90335	783.1224
8.2	2.095506	105.8338	99.90335	754.0799
10.2	2.126626	105.9967	99.90335	727.2561
11.9	2.025743	105.7026	99.90335	691.9511
16.0	1.346949	103.1624	99.90335	597.5426

Table A.4: Fitting parameters for copper, pump DBR at 10 °C

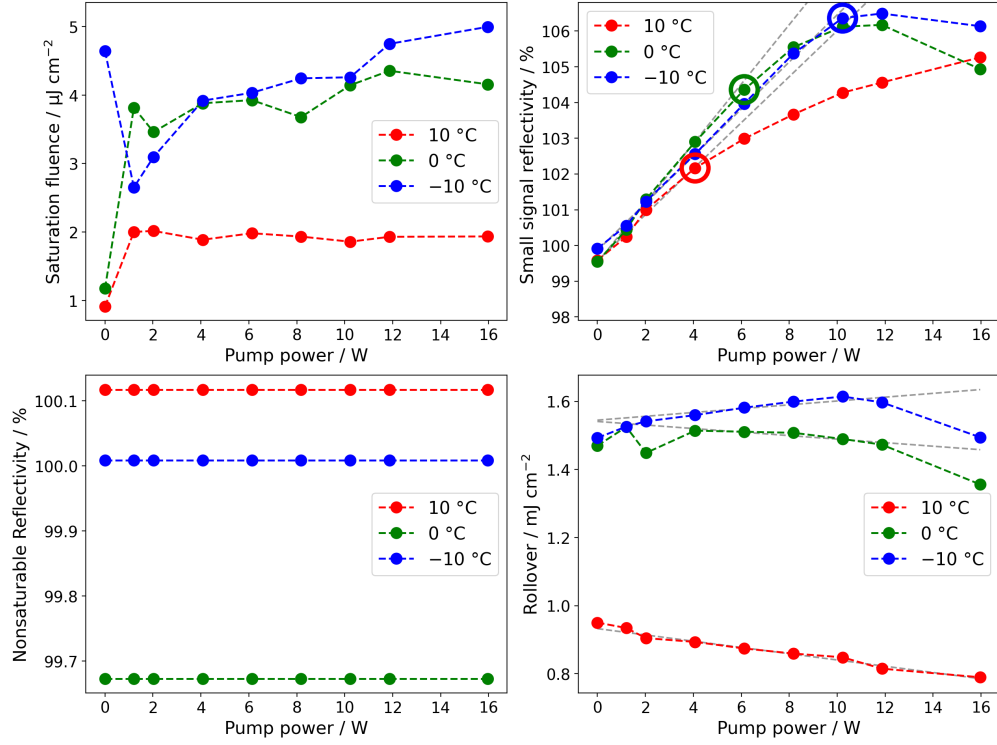
Power / W	F_{sat} / μJcm^{-2}	R_{ss} / %	R_{ns} / %	F_2 / μJcm^{-2}
0.0	0.5080624	98.33377	98.80948	1186.357
1.2	6.175294	99.05014	98.80948	1209.883
2.0	3.331011	99.69253	98.80948	1223.63
4.1	3.234527	100.9742	98.80948	1215.72
6.1	2.999036	102.2298	98.80948	1205.156
8.2	2.908727	103.4118	98.80948	1188.482
10.2	2.95707	104.1216	98.80948	1167.011
11.9	2.961998	104.3594	98.80948	1159.052
16.0	2.455654	103.534	98.80948	1085.153

Table A.5: Fitting parameters for copper, pump DBR at 0 °C

Power / W	F_{sat} / μJcm^{-2}	R_{ss} / %	R_{ns} / %	F_2 / μJcm^{-2}
0.0	0.3754365	98.48692	98.81127	1314.791
1.2	7.111296	99.0651	98.81127	1328.366
2.0	4.181167	99.47393	98.81127	1349.31
4.1	3.384677	100.4257	98.81127	1362.225
6.1	3.292022	101.4668	98.81127	1339.622
8.2	3.222231	102.5786	98.81127	1331.669
10.2	3.194545	103.7065	98.81127	1312.843
11.9	3.229795	104.2893	98.81127	1303.142
16.0	3.136977	104.6044	98.81127	1236.418

Table A.6: Fitting parameters for copper, pump DBR at −10 °C

A.1.3 Diamond, pump DBR VECSEL



Power / W	$F_{sat} / \mu\text{Jcm}^{-2}$	$R_{ss} / \%$	$R_{ns} / \%$	$F_2 / \mu\text{Jcm}^{-2}$
0.0	0.9116372	99.58587	100.1174	950.5124
1.2	2.000422	100.2428	100.1174	934.6019
2.0	2.015472	100.9966	100.1174	904.7597
4.1	1.886598	102.1674	100.1174	893.6754
6.1	1.981396	102.9881	100.1174	874.374
8.2	1.932478	103.6679	100.1174	859.4888
10.2	1.857932	104.277	100.1174	848.525
11.9	1.929301	104.5611	100.1174	815.1581
16.0	1.93455	105.2651	100.1174	789.8177

Table A.7: Fitting parameters for diamond, pump DBR at 10 °C

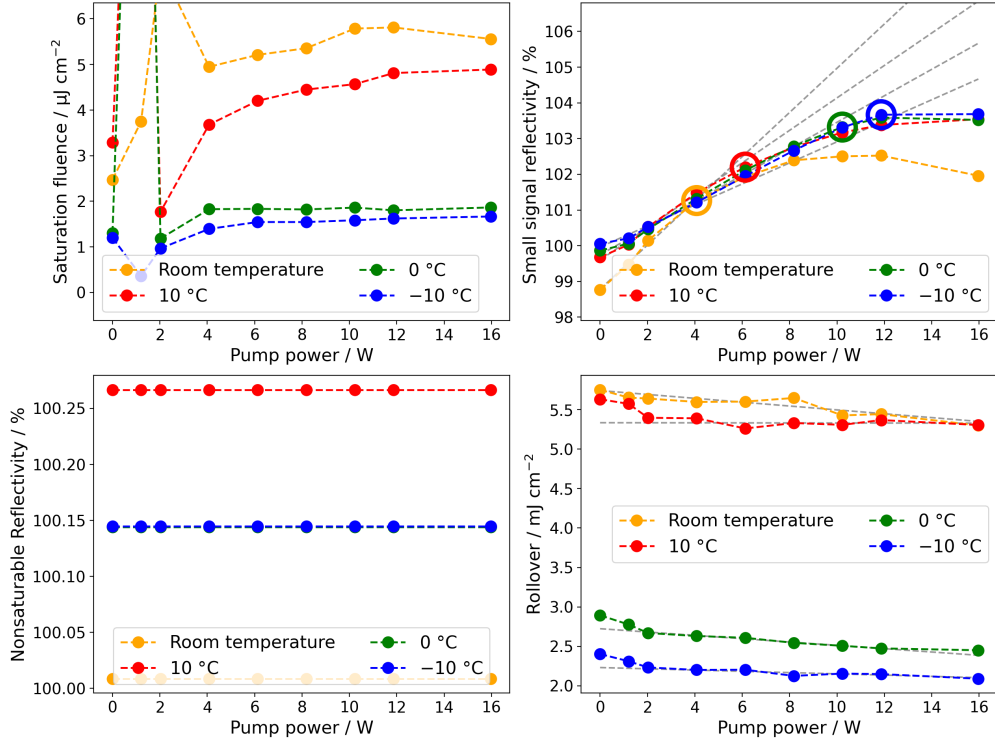
Power / W	F_{sat} / μJcm^{-2}	R_{ss} / %	R_{ns} / %	F_2 / μJcm^{-2}
0.0	1.173952	99.54422	99.673	1470.144
1.2	3.815373	100.441	99.673	1525.138
2.0	3.459009	101.2913	99.673	1448.873
4.1	3.878965	102.8989	99.673	1514.299
6.1	3.925065	104.3614	99.673	1511.086
8.2	3.67713	105.5481	99.673	1507.975
10.2	4.141628	106.1223	99.673	1489.837
11.9	4.353316	106.1732	99.673	1473.182
16.0	4.155071	104.9347	99.673	1356.259

Table A.8: Fitting parameters for diamond, pump DBR at 0 °C

Power / W	F_{sat} / μJcm^{-2}	R_{ss} / %	R_{ns} / %	F_2 / μJcm^{-2}
0.0	4.640948	99.9132	100.0084	1493.049
1.2	2.651343	100.5562	100.0084	1526.21
2.0	3.094484	101.232	100.0084	1541.714
4.1	3.916732	102.5598	100.0084	1559.89
6.1	4.031945	103.9692	100.0084	1581.835
8.2	4.242787	105.3714	100.0084	1599.612
10.2	4.258473	106.3635	100.0084	1614.561
11.9	4.746326	106.4912	100.0084	1597.418
16.0	4.995075	106.1361	100.0084	1494.667

Table A.9: Fitting parameters for diamond, pump DBR at −10 °C

A.1.4 Hybrid VECSEL



Power / W	$F_{sat} / \mu\text{Jcm}^{-2}$	$R_{ss} / \%$	$R_{ns} / \%$	$F_2 / \mu\text{Jcm}^{-2}$
0.0	3.290619	99.67631	100.2666	5631.471
1.2	17.83833	100.0312	100.2666	5573.312
2.0	1.768194	100.5271	100.2666	5396.711
4.1	3.680214	101.4798	100.2666	5390.342
6.1	4.202757	102.201	100.2666	5261.749
8.2	4.44895	102.7604	100.2666	5330.434
10.2	4.567745	103.1701	100.2666	5307.421
11.9	4.811489	103.38	100.2666	5367.859
16.0	4.888468	103.5434	100.2666	5305.489

Table A.10: Fitting parameters for hybrid at 10 °C

Power / W	$F_{sat} / \mu Jcm^{-2}$	$R_{ss} / \%$	$R_{ns} / \%$	$F_2 / \mu Jcm^{-2}$
0.0	1.302447	99.86569	100.1441	2893.923
1.2	20.0	100.0583	100.1441	2777.417
2.0	1.183295	100.4638	100.1441	2669.408
4.1	1.826213	101.3199	100.1441	2631.553
6.1	1.833277	102.1102	100.1441	2609.214
8.2	1.820321	102.788	100.1441	2545.14
10.2	1.860575	103.3222	100.1441	2507.481
11.9	1.801447	103.5872	100.1441	2474.857
16.0	1.864217	103.5233	100.1441	2451.36

Table A.11: Fitting parameters for hybrid at 0 °C

Power / W	$F_{sat} / \mu Jcm^{-2}$	$R_{ss} / \%$	$R_{ns} / \%$	$F_2 / \mu Jcm^{-2}$
0.0	1.199973	100.058	100.1446	2403.644
1.2	0.3623746	100.206	100.1446	2311.655
2.0	0.9666645	100.5291	100.1446	2233.357
4.1	1.393968	101.2126	100.1446	2202.014
6.1	1.544497	101.9515	100.1446	2204.409
8.2	1.543916	102.6669	100.1446	2126.512
10.2	1.583621	103.312	100.1446	2155.628
11.9	1.621696	103.668	100.1446	2149.006
16.0	1.665911	103.6861	100.1446	2090.695

Table A.12: Fitting parameters for hybrid at −10 °C

Power / W	$F_{sat} / \mu Jcm^{-2}$	$R_{ss} / \%$	$R_{ns} / \%$	$F_2 / \mu Jcm^{-2}$
0.0	2.471605	98.7645	100.0087	5751.834
1.2	3.747762	99.47048	100.0087	5652.824
2.0	7.137965	100.1484	100.0087	5640.555
4.1	4.948034	101.2644	100.0087	5597.407
6.1	5.210384	101.9301	100.0087	5602.011
8.2	5.35578	102.3919	100.0087	5647.915
10.2	5.786727	102.5033	100.0087	5427.009
11.9	5.811465	102.5235	100.0087	5443.254
16.0	5.559201	101.9594	100.0087	5299.027

Table A.13: Fitting parameters for hybrid at Room temperature